Mn, Fe, Zn and As speciation in a fast-growing ferromanganese marine nodule.

Matthew A. Marcus, Alain Manceau, Michael Kersten

Mn, Fe, Zn and As speciation in a fast-growing ferromanganese marine nodule

Matthew A. Marcus[1], Alain Manceau[2] and Michael Kersten[3]

[1]Advanced Light Source, Lawrence Berkeley Laboratories, 1 Cyclotron Road, Berkeley CA USA 94720

[2]Environmental Geochemistry Group, LGIT, University J. Fourier and CNRS, BP 53, 38041 Grenoble Cedex 9, France

[3] Geoscience Institute, Johannes Gutenberg-University, D-55099 Mainz, Germany

Corresponding author: M. Marcus, E-mail: mamarcus@lbl.gov

Keywords: XAS, EXAFS, marine ferromanganese nodule, Baltic sea, speciation

Running Title: Mn, Fe, Zn, and As speciation in ferromanganese nodule

ABSTRACT

The speciation of Mn, Fe, As and Zn in a fast-growing (0.02mm/yr), shallow-marine ferromanganese nodule has been examined by micro X-ray fluorescence, micro X-ray diffraction, and micro X-ray absorption spectroscopy. This nodule exhibits alternating Fe-rich and Mn-rich layers reflecting redox variations in water chemistry. Fe occurs as two-line ferrihydrite. The As is strictly associated with Fe and is mostly pentavalent, with an environment similar to that of As sorbed on or coprecipitated with synthetic ferrihydrite. The Mn is in the form of turbostratic birnessite with ~10 % trivalent manganese in the layers and probably ~8 % corner-sharing metal octahedra in the interlayers. The Zn is enriched on the rim of the nodule, associated with Mn. The Zn is completely (>90 %) tetrahedrally coordinated and sorbed in the interlayers of birnessite on vacant layer Mn sites. The Zn and Mn species are similar to ones found in soils, suggesting common structural principles, despite the differing formation conditions in these systems.

1. INTRODUCTION

Low sedimentation rates, erosional conditions, and seasonal redox cycling favor the formation of ferromanganese concretions at shallow water localities of the SW Baltic Sea (Glasby et al., 1997; Hlawatsch et al., 2002a). These Baltic Sea ferromanganese nodules show an onion-like growth pattern of alternating Fe- and Mn-rich layers. This pattern has been attributed to seasonal cycling variations in bottom water conditions (Hlawatsch et al., 2002a). Yearly development of summer anoxia in bottom waters leads to diagenetic remobilization from sediments, lateral transport, and diagenetic enrichment of both Mn and Fe in the concretions. Heuser (1988) found seasonally-varying growth rates which were highest from spring to autumn when the water column was stratified. In spring, at the beginning of stratification, the Mn flux to the nodule exceeds that of Fe due to decreasing oxygen concentration in the bottom waters leading to suboxic conditions. Mn^{4+} from the sediment gets reduced to Mn^{2+} before Fe^{3+} is reduced since the Mn^{4+}/Mn^{2+} couple has a higher redox potential than the Fe^{3+}/Fe^{2+} couple. On the other hand, during summer, the Fe flux may exceed that of Mn due to increasing anoxia in the bottom water, so partial dissolution of the Mn-rich layer deposited in spring may occur. In autumn, the Mn concentration in the bottom waters rises again due to the wind-induced breakup of the stratification. In addition to seasonal cyclicity, long-term (decadal) changes in the extent of summer anoxia influence the diaganetic precipitation/redissolution processes leading to an alternating Fe/Mn oxide banding much wider than the net 10–20 µm/year growth rates determined by radiometric $^{226}Ra_{ex}$/Ba profiling (Liebetrau et al., 2002). The ultimately preserved

Mn/Fe growth zonation provides rather a record of chemical changes in the environment of concretion formation. The implication that these oxide layers provide a continuously growing substrate with constant sorption efficiencies for trace elements is the basis of a continuing interest in these concretions focusing on their possible use in retrospective long-term monitoring of climate change and anthropogenic pollution (Glasby et al., 1997; Hlawatsch et al., 2002b). This method depends on the assumption that the sorbent-pollutant complex is stable once formed, with constant sorption efficiencies for trace elements. It is therefore of interest to understand the speciation of trace elements and their hosts, and whether preferential sorption on specific phases may change this record. Although a vast amount of literature exists on trace element inventory of diagenetic ferromanganese nodules, the knowledge on their geochemical speciation is still rather limited. These nodules have much in common with some other banded ferromanganese systems such as soil nodules (Palumbo, et. al., 2001; Manceau, et. al., 2003). It is therefore interesting to compare these different systems to see if there are common features.

In this paper, we examine the speciation of Mn, Fe, Zn, and As in one of these Baltic Sea nodules. Since this is one of the concretions studied by Hlawatsch et. al. (2002a,b; they labeled it MB4) and Liebetrau et al. (2002, labeled TL-2 in their Fig. 3), we have ample information about how the sample was formed, its anisotropic growth pattern, and its trace element inventory. Both Zn and As are known to be enriched in the diagenetic ferromanganese concretions, from natural as well as anthropogenic sources, and have a well known but different water chemistry. Synchrotron-based X-ray microdiffraction, as well as X-ray fluorescence and absorption microspectroscopy results presented here have given detailed insights into As and Zn phase association and speciation. The results will be discussed with respect to the geochemical enrichment processes, and with those of other banded Fe-Mn systems in the literature. We find

that the Mn-rich material is turbostratic birnessite, and that the Zn is associated with and sorbed to it. The Fe-rich material is 2-line ferrihydrite, and the As is associated with and sorbed to it. Both trace-element species (Zn,As) form similar sorption complexes as in other natural systems.

2. MATERIALS AND METHODS

As stated above, the sample is a slice of the MB4 nodule referred to in the Hlawatsch (2002a,b) papers. For reader convenience, we will recapitulate the details of the sample collection and preparation procedures. The sample was one of several ferromanganese crusts collected from a typical sub-aqueous glacial till (boulder clay) rise exposed at water depths of 20-25 m in the Mecklenburg Bight of the SW Baltic Sea ("Blinkerhügel" sampling site, 54°10´N, 11°21´E). They were found on boulders accumulated at the erosional boundary between till hills and surrounding mud, growing just above the cm-thick fluffy layer around the boulders like tree mushrooms. The fluffy layer appears to be the major redox-driven transport belt for the trace elements accumulated in the encrustations (Hlawatsch et al., 2002a). All samples were carefully collected manually by scuba divers. After collection, the samples were soaked in about 500 mL Milli-Q water, rinsed to remove sea salt, and oven-dried at 60 °C. The sample used in the present study was discoidal in shape, with a thickness of about 1cm and a diameter of 5-9 cm (short and long axes). The sample was cut in half along its longest axis to obtain a cross section in direction of its highest accretion rate (cf. Fig. 2 in Hlawatsch et al., 2002b, or Fig. 3 in Liebetrau et al., 2002). A 1mm-thick slice was embedded in Araldite resin, polished and mounted on Kapton tape for X-ray analysis.

The XRF (X-ray fluorescence), micro-XRD (X-ray diffraction), and micro-EXAFS (extended X-ray absorption fine structure) measurements described here were performed on Beamline 10.3.2 at the Advanced Light Source. This beamline provides a beam of hard X-rays adjustable from 5 x 5 μm up to 16 (H) x 7 (V) μm size. XRF shows chemical associations, e.g. between trace and major elements, which then allows us to select points of interest on which to do XRD, which tells us what the dominant minerals are in the probed volume, and EXAFS, which yields information about the local atomic environments of trace and major constituents. This beamline is described in Manceau et. al. (2002a). We also performed area-averaged EXAFS measurements at the Zn and As K-edges using a 1.5 (V) x 0.5 (H) mm^2 size beam on the FAME (BM 30B) beamline at the ESRF (European synchrotron radiation facility).

Microdiffraction was performed with a Bruker 6000 CCD at a distance of 8.2 cm from the sample. The beam energy was 14 keV, which was high enough to go through the sample and to provide access to reflections with d-spacings down to 1.06 Å. Patterns were recorded for 10 minutes with a beam size of 16 (H) x 7 (V) μm. Patterns were calibrated and integrated using Fit2d (Hammersley et al., 1996), with calibration data from LaB_6 powder.

For the Mn K-edge, laterally resolved (micro-beam) spectra were taken at six different places on the sample, with various Mn/Fe ratios. No significant difference was found between the spectra, so they were averaged together for further analysis. Micro-EXAFS Zn data were only taken at one point. However, the mapping results showed that Zn was only found where there was Mn. Since the Mn was all the same species, as seen in Mn micro-EXAFS, we inferred that the Zn is always in the same structural environment, a hypothesis which was verified by recording also an area-averaged Zn-EXAFS spectrum on FAME. A Mn spectrum taken at a point

on which the micro-beam had been sitting hours showed the effect of significant reduction of Mn^{4+} to Mn^{2+} due to radiation damage. However, no changes were noted in the individual Mn micro-EXAFS spectra because a given spot was not probed for more than half an hour. Similarly, no changes were noted in the individual Zn micro-EXAFS spectra, but hour-long exposures in the FAME beamline caused changes in the Zn EXAFS, which may be related to the changes in the Mn EXAFS mentioned above.

Mn XANES was not analyzed for valence state information because the spectra were significantly distorted by over-absorption, to which the analysis of an Mn^{3+}/Mn^{4+} mixture is sensitive. The EXAFS analysis relies mostly on distances instead of amplitudes, so is less affected by over-absorption. Zn XANES spectra were not recorded either because the XANES from Zn depends on the detailed structure and bonding and not directly on such simple measures as the octahedral/tetrahedral ratios.

EXAFS analysis was done using fluorescence data reduced to $k^3\chi(k)$ by the same methods as were used for the references. Linear fits of the unfiltered data and non-linear fits of filtered shells were done with no adjustment of E_0, as none seemed necessary. The E_0 value was taken to be the half-edge-jump point. The rationale for this choice is discussed in Manceau et. al. (1996, 2002a). For some of the work, FEFF 8.10 (Ankudinov et al., 1998) was used to generate theoretical amplitude and phase shift functions. The deglitching, reduction to *k* space and fitting were done with the homebrew software available on ALS Beamline 10.3.2. This software is similar to WinXAS and has been found to produce similar results. Briefly, the pre-edge was fit to a linear function and subtracted, and the post-edge was fit to a cubic spline, which was used for subtraction and normalization. Care was taken to ensure that the short-distance As-O shells were

not unduly affected by the post-edge spline. The Fourier transforms were done on the entire $k^n\chi(k)$ curves shown in Figures 6, 9 and 11 under a Kaiser-Bessel window (β=2.5).

3. RESULTS AND DISCUSSION

3.1. XRF mapping

XRF mapping was done at a pixel size of 5 μm, yielding results consistent with Figure 3 of Hlawatsch et. al. (2002b). Such a map is shown in Figure 1 as a tricolor picture. In this Figure, each pixel is colored red in proportion to the Zn signal, blue in proportion to Fe, and green in proportion to Mn. Pixels corresponding to points with more than one element show colors derived by adding together red, green and blue colors in proportion to the amounts of Zn, Mn and Fe, respectively. The Fe/Mn banding shows as a blue/green alternation. The bands are widest at the right-hand edge of Figure 1. This surface represents the edge of the nodule, along the sediment-water interface. Liebetrau et. al. (2002) showed that this type of nodule grows fastest along the sediment-water interface, as shown in their Figure 3. The Zn is associated with Mn and mostly on the rim, thus leading to the yellow-orange colors in Figure 1.

Positive-contrast grayscale maps for Zn, Mn and Fe are shown separately below the color map. The previous analytical work (Hlawatsch et al., 2002b) showed that the average Zn concentration in the outer 2 mm of the nodule is about 0.1 mg/g. To make the relations between the three elements clearer, we show scatterplots for the above map in Figure 2. These plots are graphs of the counts of one element plotted against those for another, with each pixel in Figure 1 contributing one point. Scatterplots are shown for Zn vs. Mn, Zn vs. FeK_β (the FeK_α contains a

small contribution from MnK_β), and Mn vs. FeK_β. The Zn-Mn plot demonstrates that where there is Zn, there is also Mn. The discrete "rays" in the scatterplot may be traced to bands in the map. That these bands show up as rays of differing slopes shows that the [Zn]/[Mn] ratio differs from band to band. Closer examination shows that the [Zn]/[Mn] ratio is highest for the surface bands at the edge where the growth rate is highest. As we will show below, the speciation of Mn and Zn do not change from band to band, so it is difficult to explain the observed patterns without supposing that the Zn concentration in the water was highest in recent years, which would be a signature of anthropogenic influence. The Zn-Fe and Mn-Fe plots show the anticorrelation between Fe and Mn, demonstrating that where Fe is concentrated, Mn and Zn are not and vice versa.

The Pb L_α fluorescence energy is nearly the same as the As K_α fluorescence energy. Therefore, in order to separate Pb from As, one typically maps an area twice, once just above and once just below the Pb L_3 edge. The below-edge signal in the As/Pb fluorescence peak yields the As concentration, while the difference between above- and below-edge signals may be attributed to Pb. A subset of the area shown in Figure 1 was mapped in this manner. While no significant amounts of Pb were found, As did appear in the Fe-rich bands. In contrast to Zn, As was not segregated to the surface, but occurred wherever there was Fe. Figure 3 shows the As-Fe correlation in map form (inset) and as a scatterplot. The left side of the inset map is seen in the “light” of As, while the right side images Fe. Note that the left and right halves are not the same area repeated, but are left and right halves of a larger area. This picture may be thought of as one map viewed through two filters, one on each side. In both cases, the contrast is positive, i.e. bright means concentrated. The seam between the two halves is almost invisible, showing that the As and Fe patterns are nearly identical except for the intensity scale. The pixel-by-pixel

correlation coefficient between As and Fe was 0.94. The slope of the scatterplot showed that the ratio of AsK_α to FeK_α counts was 1:144, which yields a molar concentration ratio [As]/[Fe] = 0.0023, with a 20 % error bar to cover errors in the estimation of absorption coefficients and fluorescence yields.

3.2. Diffraction

Powder patterns taken from Mn-rich and Fe-rich spots are shown in Figure 4. These patterns are consistent with those reported in Hlawatsch et. al. (2002b) but clearer. The Mn-rich area show the classic pattern of turbostratic birnessite (Drits, et. al., 1997), with symmetrical (00*l*) reflections, and (*hk*0) reflections showing tails to the high-*q* side. The Fe-rich area yields a pattern consistent with two-line ferrihydrite (Carlson and Schwertmann, 1981), including the characteristic asymmetry in the sense opposite to that of the Mn phase (Drits et al. 1993). Both patterns show a broad peak centered at about q=1.37 $Å^{-1}$ (d=4.59 Å), which is likely to be due to nanocrystalline silica, a common marine species. The sharp peaks labeled ‘q’ in the Figure match quartz, which is probably detrital.

3.3. Mn EXAFS

As the diffraction results suggest, and as will be shown below, the Mn-rich phase in the nodule appears to be a member of the birnessite family of phyllomanganates. To make clearer the discussion below, we will make a short digression into the crystal chemistry of birnessites. These compounds consist of layers of edge-sharing MnO_6 octahedra with water and cations, such as transition metals, alkali and alkaline earth metal ions, between the layers. A generic layer with

various kinds of defects is shown in Figure 5. The top row contains only tetravalent Mn and no defects. If the entire layer were like that, the material would be stoichiometric MnO_2 and would not need interlayer cations to balance charge. However, such simplicity almost never occurs. The row labelled 1) contains a trivalent Mn ion substituting for an Mn^{4+}. Since Mn^{3+} is bigger than Mn^{4+}, the Mn-Mn distances around the trivalent ion will be larger than for a tetravalent site. As we shall see below, this difference can be detected by EXAFS. Row 2) contains a vacant site whose six oxygen neighbors (three above, three below) provide possible attachment points for ions in the interlayer. Row 3) includes a vacant site capped with a trivalent Mn in the interlayer. The corner-sharing neighbors of this interlayer atom will be at greater distances than those found in a purely edge-sharing layer. Row 4) is the same thing, but with the Mn^{3+} on the other side of the layer. Rows 5) and 6) show combinations of defects which can occur either at random or with ordering. The reference compounds discussed below contain these defects in various proportions. The EXAFS data analysis is intended to establish the identity of the manganese phase in the nodule as birnessite and to give some idea of what defects are present and in what quantity.

The foregoing discussion shows that these materials are complex, with many structural parameters. No two defective natural phyllomanganates are likely to have the same combination of layer stoichiometry, amount of interlayer Mn^{3+}, vacancy content, domain size, ordering, etc. Thus, it is unlikely that any surrogate will be identical to a natural compound, or even that any combination of two will be a perfect match. Further, first-principles (e.g., FEFF) simulations are difficult not only because of the large number of structural parameters just mentioned, but also because the layer and interlayer sites and the Mn^{3+} and Mn^{4+} octahedra are inequivalent. The best strategy we have devised is to do careful comparisons of samples, in both *k* and *R* spaces, with references chosen to exemplify certain structural features.

The $k^3\chi(k)$ data, averaged over six locations, is shown in Figure 6 along with patterns for a selection of birnessite references. These references come from previous work and are denoted by the code-names dBi, TcBi, KBi_{10}, KBi_8 and HBi. The first reference, dBi (Villalobos et al., 2003), is a turbostratic birnessite (δ-$H_{4y}Na_{4x}(Mn^{4+}_{1-x-y}\square_{x+y})O_2 \cdot zH_2O$, where $\square$ represents vacancies). The [Na]/[Mn] ratio 4x/(1-x-y) is 0.25, and the total vacancy content x+y is between 0.06 and 0.17 (Villalobos et. al., in preparation). No detectable trivalent Mn was found by chemical analysis. TcBi is triclinic Na-birnessite ($Na_{0.31}(Mn^{4+}_{0.69}Mn^{3+}_{0.31})O_2 \cdot 0.40H_2O$) with 31% Mn^{3+} and no Mn layer vacancies or interlayer Mn (Silvester et al., 1997; Lanson et al., 2002). KBi_{10} and KBi_8 are synthetic birnessites made from $KMnO_4$. KBi_{10} ($K_{0.30}(Mn^{4+}_{0.74}Mn^{3+}_{0.24}\square_{0.015})O_2 \cdot 0.50\ H_2O$) is similar to TcBi, but it has 24 % Mn^{3+} in the layers (Gaillot, 2002). KBi_8 contains 8 % Mn^{3+} all in the interlayers. Its structural formula, except for some possible protons, may be written as $K_{0.231}Mn^{3+}_{0.077}(Mn^{4+}_{0.885}\square_{0.115})O_2 \cdot 0.60\ H_2O$ (Gaillot et. al., 2003). The interlayer Mn is written first in this formula. Finally, HBi is a hexagonal birnessite which has more interlayer Mn than the other materials: $Mn^{2+}_{0.05}Mn^{3+}_{0.12}(Mn^{4+}_{0.74}Mn^{3+}_{0.10}\square_{0.17})O_{1.7}(OH)_{0.3}$ (Drits, et. al., 1997; Silvester et al., 1997). It has 22 % Mn^{3+} and the small amount of Mn^{2+} has little effect on the EXAFS.

All the EXAFS patterns shown have obvious likenesses. They all show a distinctive pattern of three bumps at 4-6 $Å^{-1}$, which is common to phyllomanganates (Manceau et al., 2002a). In energy space, this complex of features looks like a short, descending staircase, so we refer to this region as the "staircase". The region around 8-9.4 $Å^{-1}$ (the "indicator" region) is known to be sensitive to the amount and ordering of Mn^{3+} in the manganese layer (Manceau et al., 2004). The

top three models have no interlayer Mn and are arranged in order of increasing layer Mn^{3+}. We see an overall shift of the patterns to the left as the trivalent content increases. The bottom two models contain interlayer Mn. The effect of this component is not obvious in *k* space, but can be seen in *R* space as will be shown below. Comparing the imaginary parts of Fourier transforms (Fig. 7a) for dBi and TcBi in the 2.5 Å < $R+\Delta R$ < 3.0 Å interval, we find that there is a rightward shift of the features for the TcBi when compared with those in the all-tetravalent dBi. This phase shift may be explained with reference to the fact that the Mn^{3+} ion is bigger than the Mn^{4+} ion. Thus, the Mn-Mn distances will depend on the trivalent manganese fraction. Finally, the sample shows a smallr, but significant, leftward shift in *k* space (Fig. 6) and rightward shift in *R* space (Fig. 7a) with respect to dBi. This suggests that, while the sample has mostly tetravalent Mn, there is some trivalent Mn as well.

We can evaluate the amount of Mn^{3+} in the sample in two ways. We can filter the Mn-Mn shells and do traditional single-shell fitting, or we can attempt to fit the whole spectrum in *k* space by making weighted sums of reference spectra. The lines labeled 'Fit' in Figure 7 show the results in *R* space of doing the *k* space linear-combination fit using references having the lowest (dBi) and highest (TcBi) amounts of Mn^{3+}. This fit consists of a sum of 48 % of dBi and 21 % of TcBi. The percentages do not add to 100% because of overabsorption in the sample. This effect is difficult to correct for because the six locations at which the data were taken contained varying amounts of Fe oxides, silica and other "background" species, which reduce the effect of overabsorption. The ratio of the amplitude of the TcBi contribution to the total is 21/(21+48) = 0.31. Thus, the Mn^{3+} mole fraction is 0.31x0.31 = 9.6 %. Figure 7b shows that the fit even reproduces some of the detail in the higher shells past 5 Å. A two-component fit using KBi_8 and KBi_{10} yields an Mn^{3+} fraction of 10.6 %, showing that this method produces consistent results.

The other type of fit involves extracting individual shells and fitting to references. The results of these fits, not only for the Mn but also for Zn and As, are shown in Table 1. Since dBi is structurally similar to the sample but simpler in its lack of trivalent Mn, we used this material as a reference. Fourier-filtering the second (Mn-Mn) shell of the sample and fitting it with one shell yields a distance about 0.01 Å greater than in the dBi reference. The second-shell distance for TcBi, fitted the same way as the sample, is 0.04 Å greater than that in the dBi reference, as expected from the presence of Mn^{3+}. For the purposes of this exercise, we ignore the splitting of the second shell of TcBi (Silvester et al., 1997) and fit it as if it were single. If we fit the second shell of the sample with a sum of the second shells of dBi and TcBi, we find a good fit with 53 % of dBi and 24 % of TcBi, for a TcBi/(TcBi+dBi) fraction of 30 %, which yields an Mn^{3+} content of 9.3 %. In this fit, only the amounts of the two references were allowed to float; the energy zero ΔE_0 and Debye-Waller factor (DWF) were held fixed. Allowing the DWFs to float yielded amounts of 0.55 dBi and 0.34 TcBi. Thus, the second shells taken alone send the same message as the entire spectrum. Note that these fits detect the fraction of Mn in the layers which is trivalent, and are not sensitive to the interlayer Mn.

In these fits, it should be noted that the precision of distance determinations is considerably better than the absolute accuracy because we have references which are structurally similar to the unknown. Thus, we can see small distance differences between sample and unknown, even if we cannot measure an absolute distance to better than ~0.02 Å. The tight error bars for the sample distances in Table 1 should be understood as referring to the difference between the distances in sample and reference.

Also, it is known that when there is interlayer Mn octahedra that share corners with the layer octahedra, a peak appears in the Fourier transform magnitude of the *k*-weighted $\chi(k)$ function at $R+\Delta R \sim 3$ Å (Silvester et al., 1997; Manceau et al., 1997; Gaillot et al., 2003). We see a small peak there, as shown in Figure 8. Although this peak is small, it is in-phase with the corresponding peaks in HBi and KBi_8. The phase also matches the theory for Mn-Mn bonds at 3.49Å. The magnitude of this peak matches that in KBi_8, so we tentatively conclude that the sample has about as much interlayer metal atom (i.e., Mn, Zn) as this reference (i.e., 8 %). Similarly, we used shell-by-shell fitting in an attempt to estimate how much interlayer Mn there is. We Fourier filtered in an *R* range wide enough to include the second (intralayer Mn-Mn) and third (Mn-interlayer Mn) shells. We then fit the filtered data using the second shell of dBi as a reference. The fit converges at a coordination number of about 0.6 for the interlayer shell, which would imply an interlayer fraction of about 0.05. However, the reduction in the sum-squared residual obtained by adding this shell does not justify the additional two parameters used in the fit.

We conclude from our XRD and Mn-EXAFS investigation that the Mn is in the form of a turbostratic birnessite with about 30 % as much Mn^{3+} in the manganese layer as for TcBi, which comes to about 10 %. A small amount of corner-sharing bonding was probably detected at the Mn K-edge. Some aspects of the birnessite structure are manifested in interatomic distances greater than 5Å as well as in the first shells.

3.4. Zn EXAFS

We now pass from the realm of major elements into that of the trace elements. As stated above, we find Zn only where there is Mn, suggesting a close structural association. Since the Mn was found to be all of one species, we infer that the Zn is as well. To test this, we compared the EXAFS from a 0.5 x 1.5 mm^2 region (taken at ESRF) with that from the one spot we probed with the micro beam at ALS. We found no detectable difference between the two spectra, lending credence to our assertion that the Zn is uniformly speciated throughout the area where Zn is most prevalent (colored yellow in Figure 1).

The micro-EXAFS spectrum is shown in Figure 9 along with the spectrum for a reference, Zn-sorbed birnessite (ZnBi8, [Zn]/[Mn]=0.008). This reference is known from previous work (Manceau, et. al. 2002b) to have about 30 % of its Zn in octahedral coordination in the interlayer region, with the rest of Zn tetrahedral. We see that there is a phase shift such that the sample has a shorter distance than the reference. A look at Figure 10 shows the same effect in *R* space. The solid line shows the magnitude and imaginary part of the Fourier transform for the sample, the dashed line refers to the reference, and the dotted line is for chalcophanite ($ZnMn_3O_7 \cdot 3H_2O$), a Zn phyllomanganate in which the Zn is fully octahedral. We see that the first-shell distance for the ZnBi8 reference is between those for the sample and chalcophanite. We fitted the first shell of the sample with a mix of the first shells of two reference minerals, zincite (ZnO), which is fully tetrahedral (wurzite structure), and chalcophanite, and found that there is at most about 7 % of octahedral contribution to the first shell of Zn in the sample. Thus, we consider that all or almost all of the Zn in the nodule is tetrahedral.

The second shell of the sample shows a distinctly shorter distance than in the ZnBi8 reference. The shorter distance is understandable in the light of the Zn being mostly, if not uniquely, tetrahedral. We fitted the Zn-Mn shells using FEFF-derived amplitude and phase shift

functions for which S_0^2, σ^2, and ΔE_0 were adjusted to match the second shell of chalcophanite. This reference could not be used directly because there is a Zn-O shell at about the same distance as the Zn-Mn shell. Therefore, FEFF-generated Zn-O and Zn-Mn shells were fitted to the chalcophanite reference, and the results for Zn-Mn were used to fit the sample. The nodule shows a Zn-Mn distance of 3.33Å, while the ZnBi8 reference analyzed as one Mn shell yields a distance of 3.37Å. The sum-square residual for the nodule fit goes up threefold if we force the distance in the sample to be the same as in the ZnBi8. These results are consistent with a picture of Zn sorbed as tetrahedra sitting on vacancy sites of the Mn layers of a birnessite in which the Mn is predominantly tetravalent.

We can compare these results with those obtained by Manceau, et. al. (2003) for soil ferromanganese nodules, in which Zn is found to be sorbed not only on birnessite, but on goethite and phyllosilicate as well. Like the present sample, soil nodules are formed in the presence of an oscillating redox potential, which results in a more or less regular alternate deposition and dissolution of Mn oxide. In the soil nodules studied in the cited paper, the [Fe]/[Mn] ratio is not very different from that in the marine nodule, but the Fe is in the form of goethite rather than ferrihydrite. Since ferrihydrite has a higher surface area than goethite (Spadini et al., 1994), it is somewhat surprising that the Zn does not sorb on the Fe oxide in the Baltic sample when it does in soil. A likely explanation was given by Hlawatch et. al. (2002a): During the more-anoxic summer periods during which the Fe was deposited, the fluffy layer of sediment on which the nodule sat was anoxic and scavenged Zn by reaction with sulfides which dramatically decreased the Zn flux to the nodule environment. On the contrary, during the part of the cycle during which Mn was deposited, the fluffy layer was less anoxic and released Zn into the bottom water where it became available for incorporation into the oxides being formed. Thus, the fact that Zn is

associated with Mn and not with Fe may not result from the relative affinities or sorption capacities of the various host minerals for Zn, but rather from the chemistry of the solution at the times during which the metals were scavenged. Consequently, the implication that these oxide layers provide a substrate which continuously and uniformly accumulates trace elements as the basis of their possible use in retrospective long-term monitoring is clearly invalid. The Fe/Mn zoning provides for a changing sorbent/sorbate interrelation which is superimposed on any palaeoclimate proxy or pollutant record.

3.5. As EXAFS

Our second trace species is arsenic. As we saw from the Fe and As maps, As is found where and only where Fe is. Further, the [As]/[Fe] ratio is uniform, suggesting a uniform speciation for the As. Since diffraction shows that the only identifiable Fe mineral is ferrihydrite, we can suspect that As is sorbed on ferrihydrite. Figure 11 shows the EXAFS patterns for the nodule and for As coprecipitated with ferrihydrite at a molar ratio of 0.5 As/Fe. Spectra for As sorbed on ferrihydrite and As coprecipitated at a molar ratio of 0.1 As/Fe were measured also. They were indistinguishable from and noisier than the one shown. Figure 11 shows a distinct likeness of the two spectra, but there is also a phase shift. The Fourier transforms (Figure 12a) show a slight shift of the As-O first shells and a structure at longer distances which looks similar but not identical between the sample and the reference.

The first shell for the coprecipitate is essentially identical to that in the reference arsenate mineral, krautite ($Mn[H_2O][AsO_3OH]$, R = 1.69 Å, CN = 4), in which As is pentavalent. A fit to the first shell of the sample yielded a distance 0.01Å larger than that for krautite. While this shift may not seem significant, the sum-squared residual doubled when the distance was forced to the

value for krautite. Thus, it seems likely that there is an admixture of trivalent As. It might be argued that this admixture is a result of radiation damage, but successive scans showed no shift of the XANES to within 0.5eV.

To measure the possible amount of As^{3+}, we performed a two-shell fit in which krautite and As_2O_3 were taken as references. The average As-O distance was taken at 1.77 Å for As_2O_3. In the fit, the distances were fixed at their values in the reference materials, and the $\Delta\sigma^2$ values constrained to be equal. We found a trivalent fraction of about 15 %, with error limits of 7.5-22 %. These limits come from fits in which we float two parameters with 7 independent data in the filtered shell.

Figure 12 also shows the higher As-Fe shells in the 2.2 – 3.2 $R + \Delta R$ interval. To see the higher shells more clearly, we subtracted off the back-transformed, filtered As-O first shell (in k space) from sample and reference, clipped the data to 10 $Å^{-1}$ to remove the noisiest parts (Figure 12b), then did the Fourier transform on the subtracted data as shown in Figure 12c. This operation lets us use the whole data range for the first shell, but only the best parts of the data for the higher-shell contribution. It is clear that the two sets of data presented in Figures 12b,c resemble each other but are not identical. It is possible that the inferred 15 % trivalent As contribution accounts for a significant part of the difference, as this species will have its own set of As-Fe distances.

Since the higher shells of the sample and reference seem to be quite similar, and since the data for the reference is better than that for the sample, we concentrated on analyzing the second shell of the reference. Using FEFF calculations with the second (As-Fe) shell of scorodite ($FeAsO_4 \cdot 2H_2O$) as a reference, we fitted the second shell to 0.6 Fe neighbors at 2.81 Å and 3.7 neighbors at 3.27 Å, with a common $\Delta\sigma^2$ of 0.0047 $Å^2$ relative to the second shell of scorodite.

These coordination numbers and distances are close to those of Manceau (1995). In that work, the two distances were attributed to mononuclear bidentate (edge-sharing, ^{2}E) and binuclear bidentate (corner-sharing, ^{2}C) complexes, shown schematically in Figure 13. Since the sample shows similar features, we suggest that these complexes are present there as well.

The data on the nodule are not quite good enough to yield the same robust fit as for the reference, however, the Fourier transform suggests that there might be relatively more of the shorter As-Fe distance ($R+\Delta R \sim 2.5$ Å), which we interpret as due to edge-sharing complexes, in the nodule than in the reference. If there are more ^{2}E complexes, this observation might be explainable in terms of the presence of silica, which is known to sorb on the same bidentate binuclear sites as are represented by the longer As-Fe distance (Tommaseo et al., in preparation)

4. CONCLUDING REMARKS

Our diagenetic ferromanganese crust sample from the Baltic Sea, despite its compositional and spatial heterogeneity, is remarkably uniform in the speciation of the four elements studied. Every species found in this sample is one well-known from samples formed on land, even if the processes involved in its formation are different from the terrestrial samples. In particular, the Mn phase was found to be a poorly crystalline ("turbostratic") birnessite with hexagonal layer symmetry similar to what has been reported for Mn oxide formed in soils (Manceau et al., 2003, 2004) and lake sediments (Friedl et al., 1997). The As is strictly associated with Fe and is mostly pentavalent, with a ^{2}C-dominated sorbate complex similar to that of As sorbed on synthetic ferrihydrite (Waychunas et al., 1993; Manceau, 1995). The apparent occurrence of up to 15 % of both reduced As(III) and Mn(III) in the Fe and Mn phases,

respectively, suggest that bottom water stagnation may have predominated during the crust formation, with potentially significant changes in adsorption properties of the thus partially reduced Mn sorbent or As sorbate. Not much is known about thermodynamic properties of such mixed-valent "MnO_X" phases. However, it is clear that a solid solution – aqueous solution equilibrium approach is warranted to describe the Mn^{3+} ion behavior in the MnO_2 host phase which will be detailed in a forthcoming paper (Kersten and Kulik, in prep.).

We have seen from EXAFS that the Zn is tetrahedrally coordinated and sits atop the vacancy sites of the manganese layers as shown schematically at the bottom of Figure 9. Manceau, et. al. (2002b) showed that the presence of layer Mn^{3+} favors this coordination over the octahedral one for low Zn loadings because the tetrahedral Zn better compensates the layer charge deficit originating from the Mn^{3+} for Mn^{4+} substitution than the octahedral Zn. Our results for Zn and Mn EXAFS therefore reinforce each other in showing the existence of both Mn^{3+} in the layer and ^{IV}Zn in the interlayer. This argument also illustrates the importance of a detailed knowledge of the actual crystal chemistry of high-surface-area and defective host phases in the study of trace element sorption and partitioning in the environment.

Acknowledgements- We thank Y. Takahasi and two anonymous reviewers for scientific and editorial advice. We gratefully acknowledge A. P. Hammersley of the ESRF for making Fit2d available. We also acknowledge the help of the staff of the FAME beamline, and the CNRS for supporting the French-CRG program at ESRF.

REFERENCES

Ankudinov A. L., Ravel B. Rehr J. J., and Conradson S. D. (1998) Real-space multiple scattering calculation of XANES. *Phys. Rev.* **B58**, 7565-7576.

Carlson, L., Schwertmann, U. (1981) Natural ferrihydrite in surface deposits from Finland and their association with silica. *Geochim. Cosmochim. Acta* **45**, 421–429.

Drits V. A., Sakharov B. A., Salyn A. L., and Manceau A. (1993) Structural model for ferrihydrite. *Clay Minerals* **28**, 185-208.

Drits V.A., Silvester E., Manceau A., Gorskhov A.I.(1997) The structure of monoclinic Na-exchanged birnessite and hexagonal H-birnessite. Part 1. Results from X-ray diffraction and selected area electron diffraction. *Am. Mineral.* **82**, 946-961.

Friedl G., Wehrli B., Manceau A. (1997) Solid phases in the cycling of manganese in eutrophic lakes. New insights from EXAFS spectroscopy. *Geochim. Cosmochim. Acta* **61**, 275-290.

Gaillot A.C. (2002) Caractérisation structurale de la birnessite: Influence du protocole de synthèse. Ph. D. thesis, University Joseph Fourier, Grenoble, France.

Gaillot A.C., Flot D., Drits V.A., Burghammer M., Manceau A., Lanson B. (2003): Structure of synthetic K-rich birnessites obtained by high-temperature decomposition of $KMnO_4$. I. I. Two-layer polytype from a 800°C experiment. *Chem. Mater.* **15**, 4666-4678.

Glasby G. P., Emelyanov E. M., Zhamoida V. A., Baturin G. N., Leipe T., Bahlo R., and Bonacker P. (1997) Environment of formation of ferromanganese concretions in the Baltic

Sea: a critical review. In *Manganese Mineralization: Geochemistry and Mineralogy of Terrestrial and Marine Deposits* (eds. K. Nicholson, J. R. Hein, B. Bühn, and S. Dasgupta). *Geol. Soc. Spec. Publ.* **119**, 213-237.

Hammersley A.P., Svensson S.O., Hanfland M., Fitch A., N., and Häusermann D. (1996) Two-dimensional detector software: From real detector to idealized image or two-theta Scan. *High Press. Res.* **14**, 235-248.

Heuser H. (1988) Beobachtungen und untersuchungen zur genese von flachwasser-manganknollen in der Kieler Bucht (westl. Ostsee). *Rep. Geol. Paläont. Inst. Univ. Kiel* **26**, 1-135.

Hlawatsch S., Neumann T., van den Berg C.M.G., Kersten M., Harff J., and Suess E. (2002a) Fast-growing, shallow-water ferro-manganese nodules from the western Baltic Sea: origin and modes of trace element incorporation. *Marine Geol*. **182**, 373-387.

Hlawatsch S., Garbe-Schönberg C.-D., Lechtenberg F., Manceau A., Tamura N., Kulik D.A., and Kersten M. (2002b) Trace metal fluxes to ferromanganese nodules from the western Baltic Sea as a record for long-term environmental changes. *Chem. Geol*. **182**, 697-709.

Lanson B., Drits V.A., Fen Q., and Manceau A. (2002) Crystal structure of synthetic Na-rich birnessite: Evidence for a triclinic one-layer cell. *Am. Mineral.* **87**, 1662-1671.

Liebetrau V., Eisenhauer A., Gussone N., Wörner G., Hansen B.T., Leipe T. (2002) $^{226}Ra_{excess}$/Ba growth rates and U-Th-Ra-Ba systematic of Baltic Mn/Fe crusts. *Geochim. Cosmochim. Acta* **66**, 73-83.

Manceau A. (1995) The mechanism of anion absorption on iron oxides: Evidence for the bonding of arsenate tetrahedra on free $Fe(O,OH)_6$ edges. *Geochim. Cosmochim. Acta* **59**, 3647-3653.

Manceau A., Boisset, M.C., Sarret G., Hazemann J.L., Mench M., Cambier P., and Prost R. (1996) Direct determination of lead speciation in contaminated soils by EXAFS spectroscopy. *Environ. Sci. Technol*. **30**, 1540-1552.

Manceau A., Drits V. A., Silvester E., Bartoli C., and Lanson B. (1997) Structural mechanism of Co(II) oxidation by the phyllomanganate, Na-buserite. *Am. Mineral.* **82**, 1150-1175.

Manceau A., Marcus M. A., and Tamura N. (2002a) Quantitative speciation of heavy metals in soils and sediments by synchrotron X-ray techniques. In *Applications of Synchrotron Radiation in Low-Temperature Geochemistry and Environmental Science* (eds. P. A. Fenter, M. L. Rivers, N. C. Sturchio, and S. R. Sutton), 341-428. Mineralogical Society of America. Reviews in Mineralogy and Geochemistry, Vol. 49.

Manceau A., Lanson B., and Drits V.A (2002b) Structure of heavy metal sorbed birnessite. Part 3. Results from powder and polarized EXAFS spectroscopy. *Geochim. Cosmochim. Acta* **66**, 2639-2663.

Manceau A., Tamura N., Celestre R.S., MacDowell A.A., Geoffroy N., Sposito G., and Padmore H.A.(2003). Molecular-scale speciation of Zn and Ni in soil ferromanganese nodules from loess soils of the Mississippi basin. *Env.. Sci. Technol*. **37**, 75-80.

Manceau A., Marcus M. A., Tamura N., Proux O., Geoffroy N., and Lanson B. (2004) Natural speciation of Zn at the micrometer scale in a clayey soil using x-ray fluorescence, absorption and diffraction. *Geochim. Cosmochim. Acta* (in press).

Palumbo B., Bellanca A., Neri R., and Roe M.J. (2001) Trace metal partitioning in Fe-Mn nodules from Sicilian soils, Italy. *Chem. Geol.* **173**, 257-269.

Silvester E., Manceau A., and Drits V.A. (1997) The Structure of monoclinic Na-exchanged birnessite and hexagonal H-birnessite. Part 2. Results from chemical studies and EXAFS spectroscopy. *Am. Mineral*. **82**, 962-978.

Spadini L., Manceau A., Schindler P. W., and Charlet L. (1994) Structure and stability of Cd^{2+} surface complexes on ferric oxides. I. Results from EXAFS spectroscopy. *J. Coll. Interf. Sci.*, **168**, 73-86.

Villalobos M., Toner, B., Bargar, J., and Sposito G. (2003) Characterization of the manganese oxide produced by *Pseudomonas putida* strain MnB1. *Geochim. Cosmochim. Acta* **67**, 2649-2662

Waychunas G. A., Rea B. A., Fuller C. C., and Davis J. A. (1993) Surface chemistry of ferrihydrite: Part 1. EXAFS studies of the geometry of coprecipitated and adsorbed arsenate. *Geochim. Cosmochim. Acta* **57**, 2251-2269.

Table 1. Single-shell EXAFS results

Shell	R(Å)	CN
Nodule Mn-Mn	2.89 ± 0.007[a,b]	4.4[c]
dBi Mn-Mn	2.88[d]	4.2
TcBi Mn-Mn	2.92[e]	5.0
Nodule Zn-O	1.962 ± 0.015[b]	4.9
Zincite Zn-O	1.977[c]	4
Chalcophanite Zn-O	2.09[e]	5.3
Nodule Zn-Mn	3.33[a]	6.7
ZnBi8 Zn-Mn	3.37	4.9
Nodule As-O	1.700 ± 0.007[b]	4.6
Krautite As-O	1.690[c]	4

a) Error bars on absolute distances are ± 0.02Å.
b) This error bar is for the distance difference between sample and reference.
c) Error bar is ± 20 % unless otherwise specified.
d) Taken as reference, so no error bar is applicable.
e) This shell is split, but is taken as one for fitting purposes and to compare with the sample.

FIGURE CAPTIONS

Fig. 1 XRF tricolor map of a ferromanganese nodule from the Baltic sea. Zn is coded as red, Mn as green, and Fe as blue. Separate monochrome maps for Zn, Mn and Fe are shown below the color maps. These maps are presented with positive contrast (bright=high concentration).

Fig. 2 Scatterplots for Zn, Mn and FeK_β for the area shown in Figure 1. The scale limits for Zn, Mn and Fe are 7, 250 and 50 arbitrary units, respectively.

Fig. 3 Scatterplot for As and Fe in a section of the nodule. The inset shows a grayscale (positive-contrast) map in which the left side represents As and the right Fe.

Fig. 4 Powder diffraction patterns taken at 14keV at Mn- and Fe-rich spots. The wavevector Q is defined as $2\pi / d$ with d the d-spacing. Peaks labeled B and F refer to turbostratic birnessite and 2-line ferrihydrite, respectively. The peak labeled s refers to nanocrystalline silica, and those labeled q come from quartz.

Fig. 5 Schematic diagram of a layer in a generic phyllomanganate. The top row is ideal in the sense of having no defects. Row 1 includes a trivalent Mn. Row 2 contains a vacancy. Rows 3 and 4 include vacancies capped at top or bottom with trivalent Mn. Rows 5 and 6 show multiple defects in a row.

Fig. 6 Mn K-edge EXAFS for the sample (dashed lines) and five birnessite references (solid lines). Note the phase differences in the "staircase" region and the features in the "indicator" region. In this and the next two Figures, the EXAFS for the sample has been multiplied by 1.31 to compensate for overabsorption.

Fig. 7 Fourier transforms of Mn K-edge $k^3\chi(k)$ EXAFS data in Figure 6. The magnitudes and imaginary parts are shown, with the magnitude shifted up for clarity. The curves are for the sample (heavy line), fit to dBi+TcBi (light line), dBi (dotted line), and TcBi (dashed line). It should be noted that small shifts in distance are more reliably detected by looking at the imaginary part than the magnitude. The upper panel shows the first two shells, and the lower shows the higher distances. Arrows point out the phase difference in the Fourier transform in the Mn-Mn region. The pure references and imaginary parts are omitted for clarity from the lower panel.

Fig. 8 Fourier transforms of Mn K-edge $k^1\chi(k)$. The data for the sample is in dashed lines, and the models in solid lines. The position of the corner-sharing (interlayer Mn) peak is indicated.

Fig. 9 Zn K-edge EXAFS compared for the sample (solid line) and low-Zn-sorbed birnessite reference (dashed line, ZnBi8). The cartoons on the bottom show the suggested structures inferred for the sample (this work) and the ZnBi8 reference (Manceau, et. al., 2002b).

Fig. 10 Fourier transform of data for the sample and reference (solid, dashed) at the Zn K-edge. For comparison, the Zn-O shell of chalcophanite (all octahedral Zn) is shown in dotted lines. The

positions of the minima in the imaginary parts are flagged to show the differences in Zn-O and Zn-Mn distances (arrows).

Fig. 11 As K-edge EXAFS from the sample (solid) and coprecipitate (As on ferrihydrite, dashed line).

Fig. 12 Fourier transforms (FTs) of As EXAFS data in Figure 11. To make the higher shells more visible, we subtracted out a filtered first shell contribution from the *k* space data and re-did the FT for sample and reference. The FTs for the data are shown in a), the *k* space data with the first shells subtracted off are shown in b) and the FTs of the subtracted data are shown in c).

Fig. 13 Idealized structural units for As sorbed on 2-line ferrihydrite, after Manceau (1995). This diagram is meant to be qualitative only and not representative of the distances between AsO_4 tetrahedra. The O atoms shown in dotted lines are below the level of the Fe and As atoms.

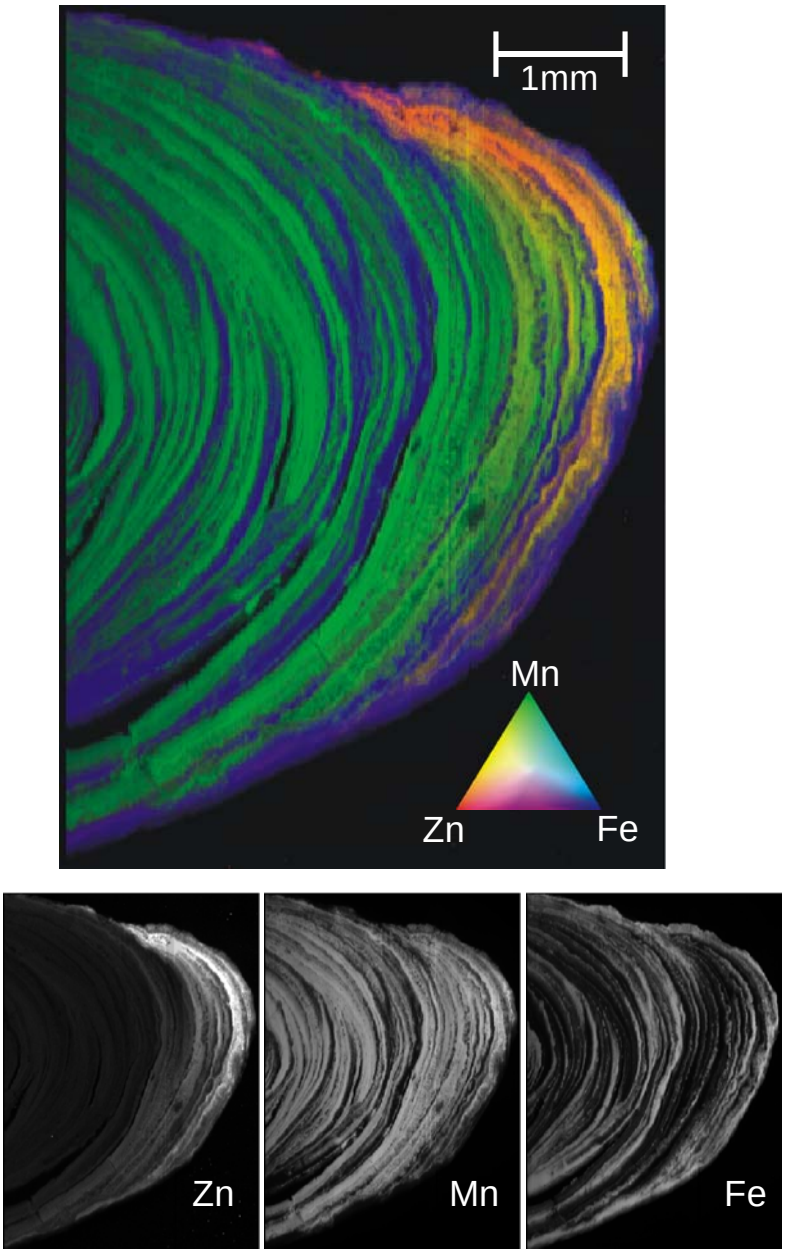

Figure 1

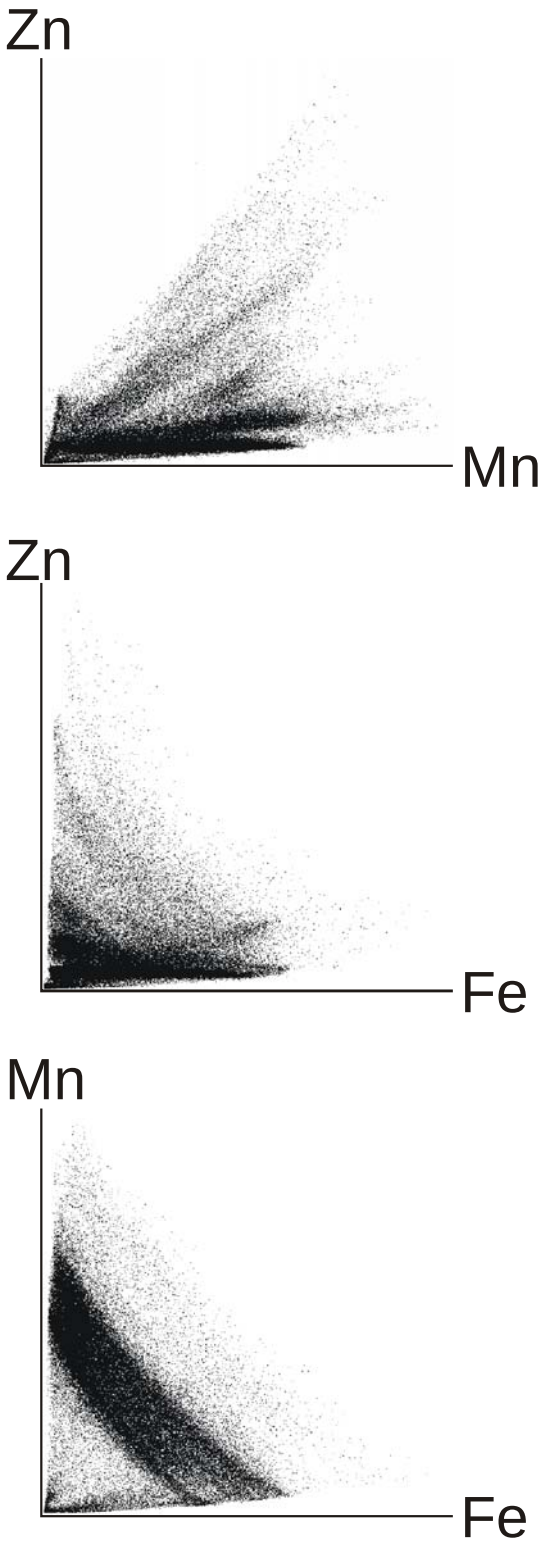

Figure 2

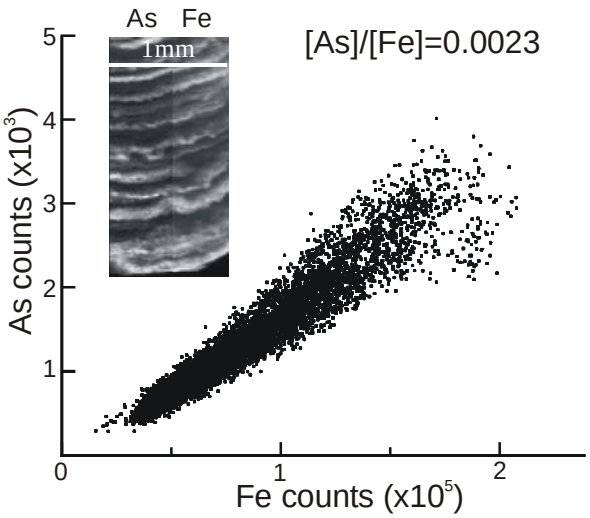

Figure 3

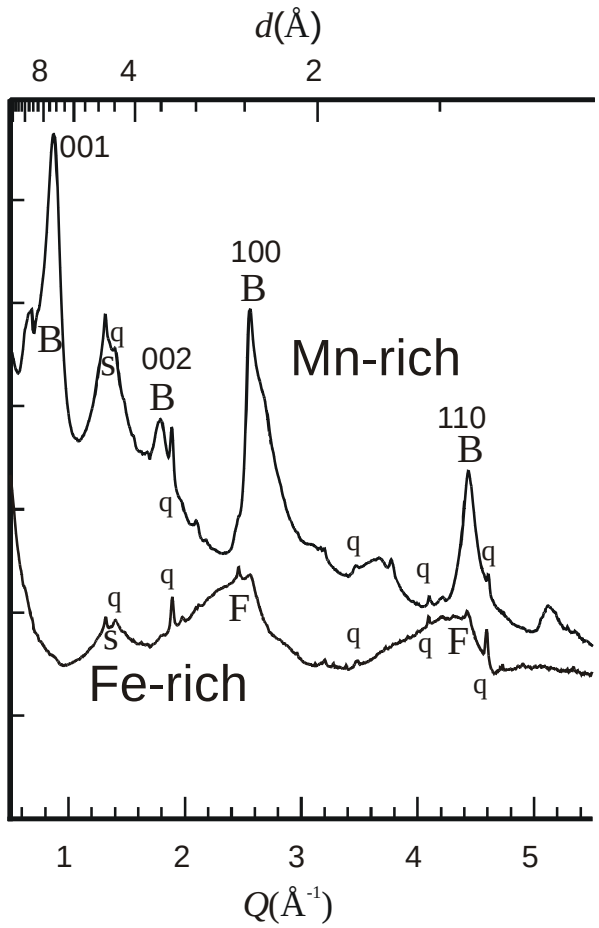
d(Å)
8
4
2
001
B
100
B
q
s
002
B
Mn-rich
110
B
q
q
q
q
q
q
F
q
s
q
q
F
Fe-rich
q
1
2
3
4
5
Q(Å-1)

Figure 4

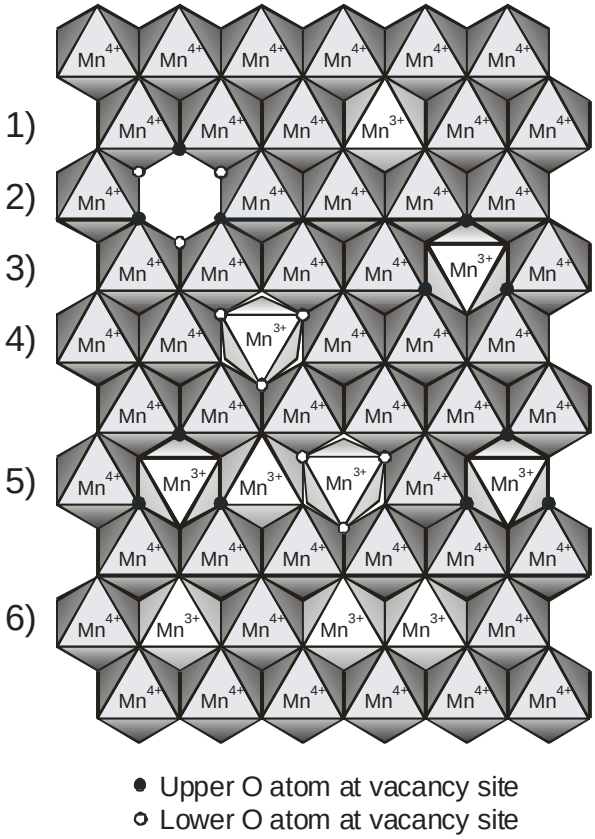
1)
2)
3)
4)
5)
6)
Upper O atom at vacancy site
Lower O atom at vacancy site

Figure 5

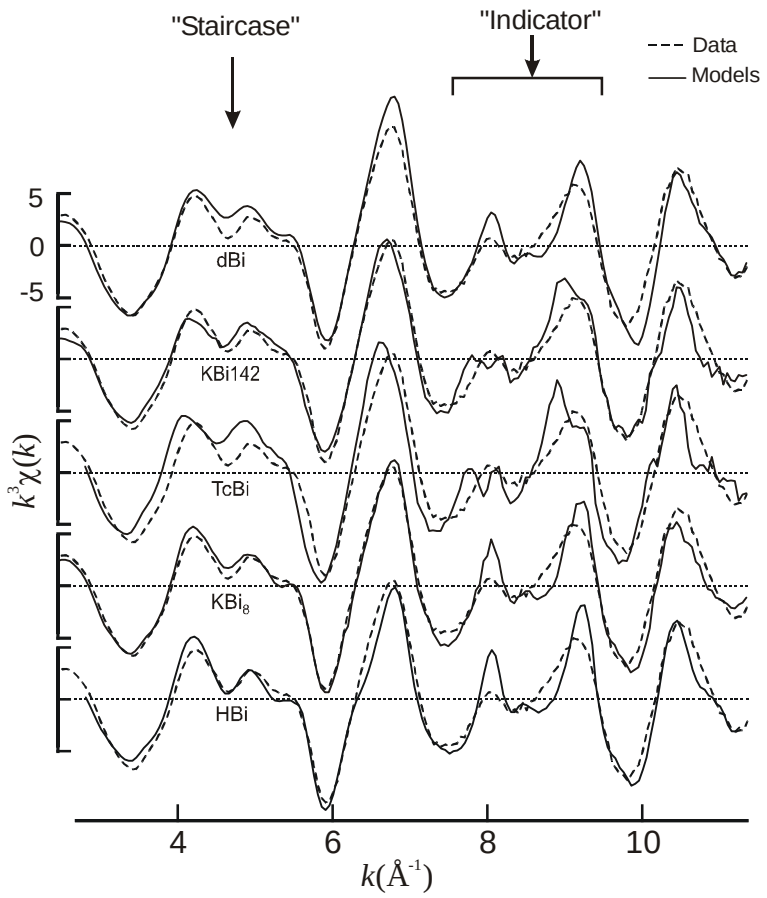
"Staircase"
"Indicator"
Data
Models
5
0
-5
dBi
KBi142
TcBi
KBi$_\theta$
HBi
$k^3\chi(k)$
4
6
8
10
k(Å^{-1})

Figure 6

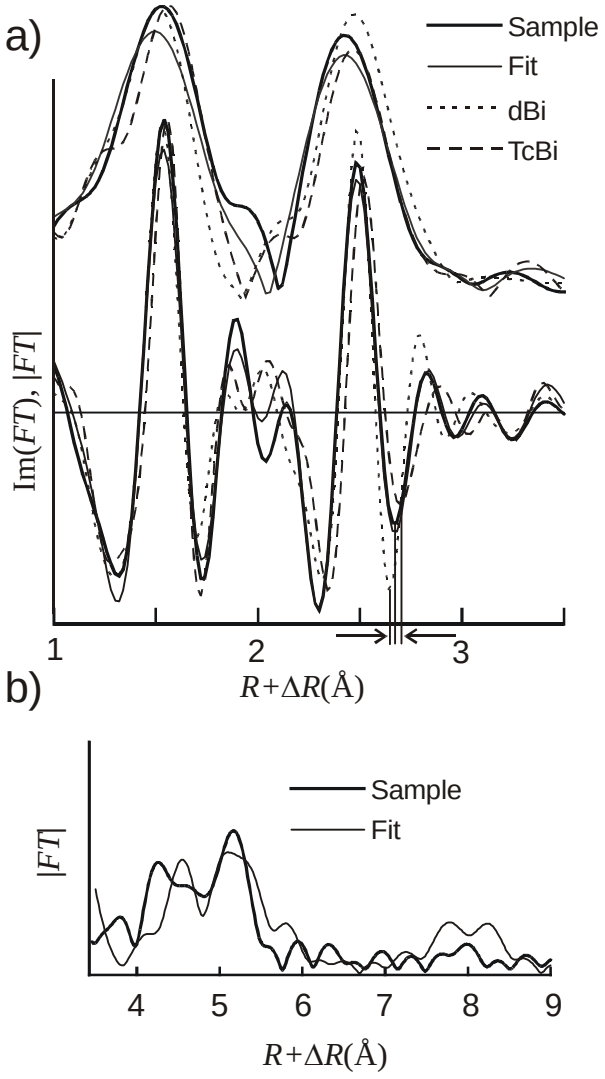
a)
Sample
Fit
dBi
TcBi
Im(FT), |FT|
1
2
3
R+ΔR(Å)
b)
Sample
Fit
|FT|
4
5
6
7
8
9
R+ΔR(Å)

Figure 7

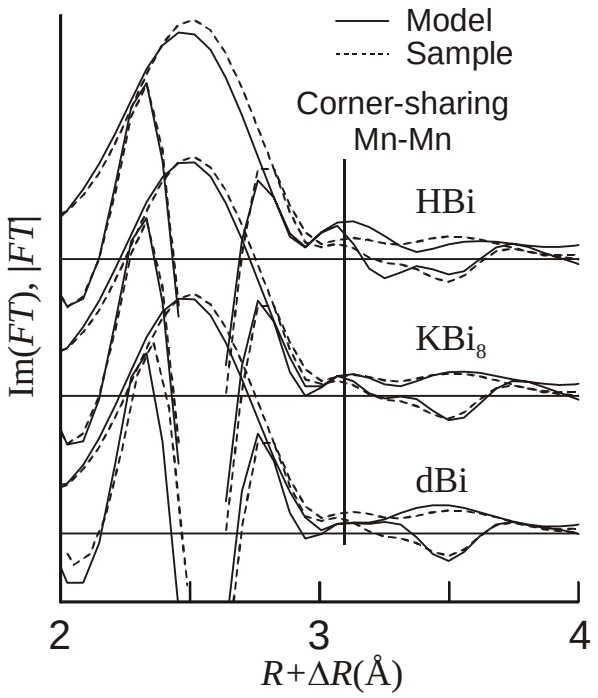
Model
Sample
Corner-sharing
Mn-Mn
HBi
KBi8
dBi
Im(FT), |FT|
2
3
4
R+ΔR(Å)

Figure 8

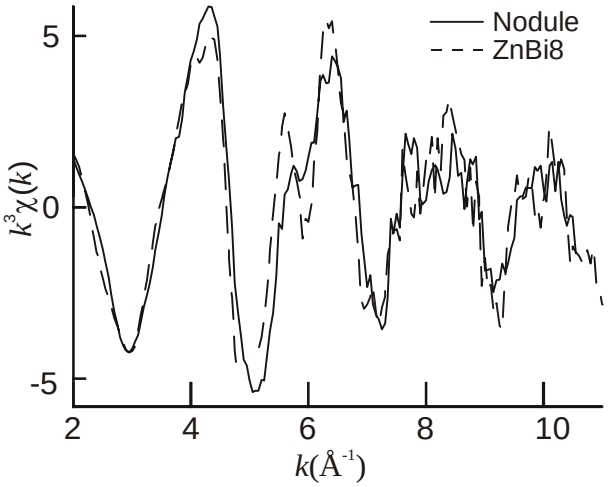
Nodule
ZnBi8
5
0
-5
2
4
6
8
10
$k^3\chi(k)$
k(Å^{-1})

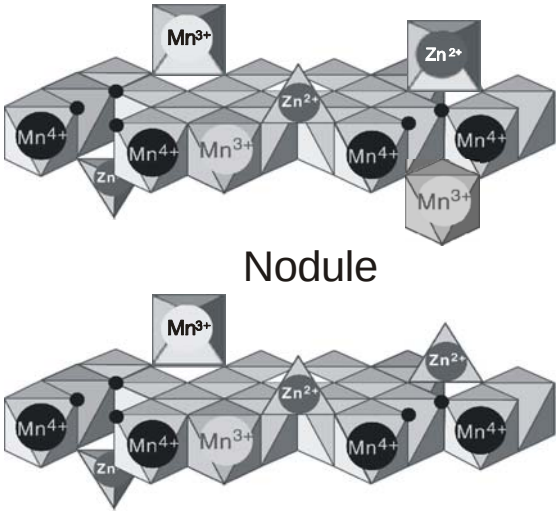
ZnBi8
Mn3+
Zn2+
Mn4+
Mn4+
Mn3+
Mn4+
Mn4+
Zn
Mn3+
Nodule
Mn3+
Zn2+
Zn2+
Mn4+
Mn4+
Mn3+
Mn4+
Mn4+
Zn

Figure 9

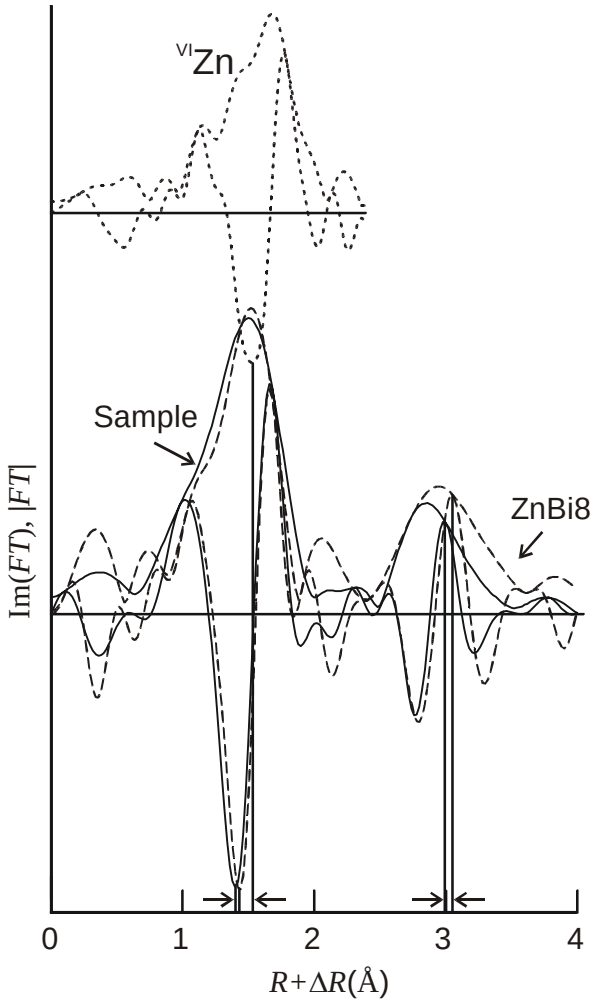

Figure 10

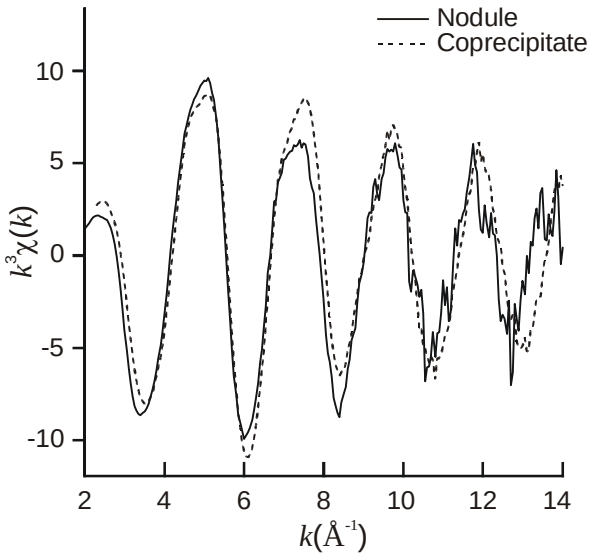

Figure 11

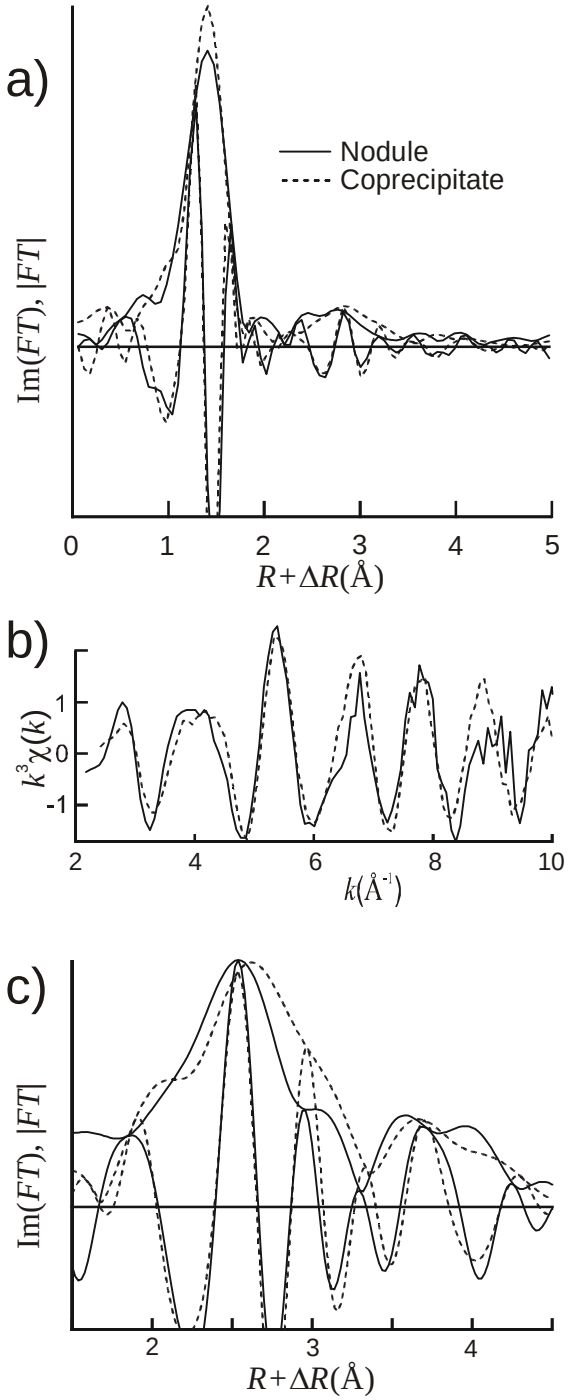
a)
Nodule
Coprecipitate
Im(FT), |FT|
0
1
2
3
4
5
R+ΔR(Å)
b)
k³χ(k)
1
0
-1
2
4
6
8
10
k(Å⁻¹)
c)
Im(FT), |FT|
2
3
4
R+ΔR(Å)

Figure 12

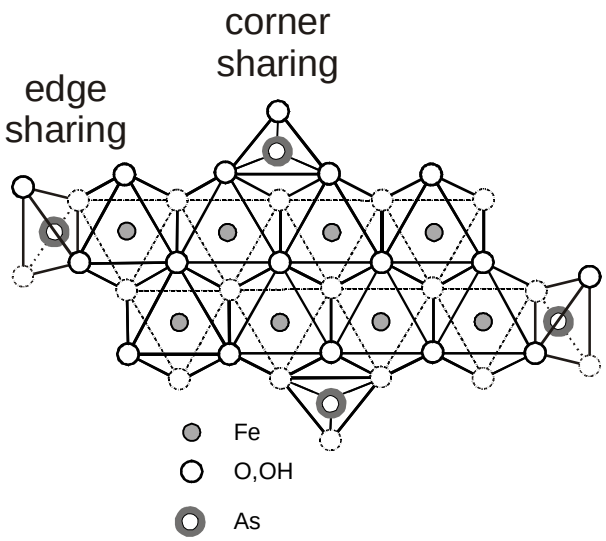

Figure 13